Atomic Layer Deposition of Pd Nanoparticles on Self-Supported Carbon-Ni/NiO-Pd Nanofiber Electrodes for Electrochemical Hydrogen and Oxygen Evolution Reactions

Ahmed Barhoum,[1,2*] Heba H. El-Maghrabi,[2,3] Igor Iatsunskyi[4], Emerson Coy[4], Aurélien Renard[5], Chrystelle Salameh[2], Matthieu Weber,[2] Syreina Sayegh,[2] Amr A. Nada[2,6], Stéphanie Roualdes[2], Mikhael Bechelany[2*]

[1] Chemistry Department, Faculty of Science, Helwan University, Cairo 11795, Helwan, Egypt

[2] Institut Européen des Membranes (IEM), UMR-5635, Univ Montpellier, ENSCM, CNRS, Place Eugène Bataillon, 34095 Montpellier, France

[3] Dept. of Refining, Egyptian Petroleum Research Institute, Cairo, Nasr city P.B. 11727, Egypt

[4]NanoBioMedical Centre, Adam Mickiewicz University, 3 Wszechnicy Piastowskiej str., 61-614, Poznan, Poland

[5]LCPME - UMR 7564 - CNRS - Université de Lorraine, 405, rue de Vandoeuvre, 54600 VILLERS-LES-NANCY, France

[6]Dept. of Analysis and Evaluation, Egyptian Petroleum Research Institute, Cairo, Nasr city P.B. 11727, Egypt

Corresponding authors: ahmed.barhoum@science.helwan.edu.eg, mikhael.bechelany@umontpellier.fr

Abstract

The most critical challenge in hydrogen fuel production is to develop efficient, eco-friendly, low-cost electrocatalysts for water splitting. In this study, self-supported carbon nanofiber (CNF)

electrodes decorated with nickel/nickel oxide (Ni/NiO) and palladium (Pd) nanoparticles (NPs) were prepared by combining electrospinning, peroxidation, and thermal carbonation with atomic layer deposition (ALD), and then employed for hydrogen evolution and oxygen evolution reactions (HER/OER). The best CNF-Ni/NiO-Pd electrode displayed the lowest overpotential (63 mV and 1.6 V at j = 10 mA cm^{-2}), a remarkably small Tafel slope (72 and 272 mV dec^{-1}), and consequent exchange current density (1.15 and 22.4 mA cm^{-2}) during HER and OER, respectively. The high chemical stability and improved electrocatalytic performance of the prepared electrodes can be explained by CNF functionalization via Ni/NiO NP encapsulation, the formation of graphitic layers that cover and protect the Ni/NiO NPs from corrosion, and ALD of Pd NPs at the surface of the self-supported CNF-Ni/NiO electrodes.

Keywords: Self-Supported Electrodes; Nickel-Palladium Catalysts; Carbon Nanofiber; Electrospinning; Atomic Layer Deposition; Hydrogen and Oxygen Evolution Reactions

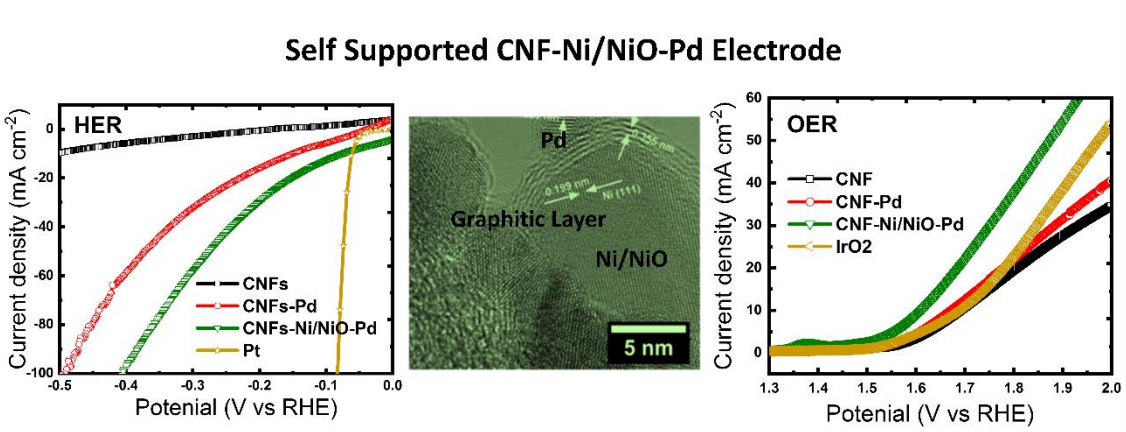

1. Introduction

Renewable energy resources have attracted considerable attention because of the global energy demand that is expected to increase in the coming decades. For instance, solar cells are used to produce electrical energy that can be converted directly into chemical energy (i.e. hydrogen fuel) through a process called electrochemical water splitting.[1,2] Hydrogen fuel is an attractive eco-friendly fuel. Indeed, it is considered a low-cost and renewable alternative source of energy to fossil fuel, with high calorimetric value and no harmful emissions in the environment.[3,4,5] It has been reported that Pt, Pt/C, IrO_2, and RuO_2, are very powerful electrocatalysts for hydrogen evolution and oxygen evolution reactions (HER/OER).[6,7] However, their commercial applications have been hindered by their high cost and rarity.[8] Therefore, the development of low-cost electrocatalysts for highly efficient HER and OER represents a pressing industrial need. To date, a large number of transition metals (e.g. Mo,[9] W,[10] Co,[11] Ni,[12] and Fe[13]) have been tested as HER and OER electrocatalysts. However, their poor chemical stability and corrosion property typically result in poor performances during HER and OER tests.[7]

Carbon nanomaterials (CNMs) have been widely used for electrochemical applications.[14,15,16,17] CNMs can promote the electron transfer reaction kinetics, enhance electrocatalyst activity, and minimize electrode surface fouling. Recently, CNMs have been used to improve the electrocatalytic activity and enhance the chemical stability of transition-metal nanoparticles (NPs) for electrochemical water splitting.[18,19] Indeed, the encapsulation of transition-metal NPs with carbon paste,[20,21] carbon nanotubes,[22] carbon nanofibers (CNFs),[23] or graphene,[24,25] significantly enhances their chemical stability and leads to higher electrochemical activity for OER, HER, and oxygen reduction reactions.[26,27,28] The interpenetrating network formed by CNFs provides numerous active sites, high electrical conductivity, mechanical stability, and allows the electrolyte high diffusion.[29,] All these unique properties make of CNFs an ideal electrode material for hydrogen fuel production,[26,27,28] water treatment,[17,30] biosensing,[31,32] batteries,[33] and fuel cells.[33] CNFs can be

prepared with various methods, such as chemical vapor deposition, template synthesis, arc discharge, laser vaporization, electrospinning, and centrifugal spinning.[33,34] Polymer electrospinning (e.g. polyacrylonitrile (PAN), polyvinylpyrrolidone, or poly(vinyl alcohol)) followed by terminal carbonization under inert atmosphere (e.g. N_2, Ar) provides a simple and versatile method to produce CNFs and their composites.[35,30,36]

CNFs are cylindrical nanostructures with graphene layers arranged as stacked cones, cups, or plates. Recently, CNF electrodes loaded with metal and metal oxide NPs with controllable compositions and high electrochemical activity have been successfully fabricated by combining electrospinning and thermal carbonization.[37,26] Combining electrospinning and thermal carbonization (peroxidation and pyrolysis) for in situ synthesis of metal NPs inside CNFs is typically more efficient than other post-synthesis techniques, such as hydrothermal synthesis, ultrasonic synthesis, UV-reduction, and microwave synthesis.[36,38] Post-synthesis techniques are performed usually using harsh oxidative processes, or modification with surfactant. They typically result in the degradation of CNF mechanical properties and electrical conductivity because of the introduction of a large number of defects in the CNFs or/and deposition of surfactant shells. However, in in situ synthesis, the polymer (PAN) domains are converted into graphitic carbon, whereas the sacrificial phase is volatilized. Moreover, the presence of metal salts (e.g. transition-metal acetate) can significantly affect the orientation of the graphite layers and increase the crystallinity of the produced CNFs.[14] It has been demonstrated that for the in situ synthesis of transition-metals NPs, Ni,[37] Mo,[28] Cu, and [26] Fe efficiently increase CNF electrical conductivity.[39] The morphologies and the dispersion of the metal NPs into/onto CNFs can be controlled by tuning the metal slat-to-polymer ratio.[35] Transition-metal NPs supported on three types of CNFs (platelet, tubular, herringbone) and nitrogen-doped CNFs can be fabricated by pyrolysis of metal carbonyl clusters and alkene complexes.[40] The size of the immobilized metal NPs can be controlled, and their location (e.g., on the edge of the graphite

layers, in the tubes and on the surface, and between the layers and on the edge) is dependent on the CNF nanostructure.[40]

Atomic layer deposition (ALD) is a thin film deposition technique that allows the preparation of inorganic layers with extreme control of their nanoscale thickness,[41] and excellent conformality of the deposits on challenging substrates, a feature that is a unique to ALD.[42] Therefore, ALD has been very useful in many different areas, such as microelectronics,[43] but also membranes,[44,45] photovoltaics,[46] and biosensing.[43] A typical ALD process is based on successive pulses of a precursor and reactant gaseous molecules, separated by pump or purge steps.[47] This process also allows precisely controlling the growth of metallic NPs, and the inclusion of doping agents.[48] Therefore, ALD has become a promising strategy for the uniform deposition of monodispersed metal NPs on a solid support with controllable particle size, size distribution, and morphology.[16,49,50] To date, ALD has been used for a wide range of catalysis applications for different types of chemical reactions, because it allows the synthesis of monometallic,[51,52] bimetallic,[53] and core–shell[54,55] noble-metal NPs. ALD is a particularly suitable technique for depositing expensive precious metals, such as Pt, Au, Pd, and Ag, because it requires low amount of metals, thus making the process cost-effective.[56,57] ALD has been widely used to deposit noble-metal NPs on CNF electrodes for electrocatalytic applications,[58,59,60] but only few studies have investigated its potential for preparing self-supported CNF electrodes for simultaneous HER and OER. Moreover, the impact of the morphology of bimetallic and core-shell junctions and nanointerfaces on CNF electrocatalytic activity has not been understood yet and is largely unexplored.

Despite the enormous efforts made, the electrocatalytic activity of earth-abundant metals is still low compared with IrO_2, RuO_2 or Pt catalysts.[61] Therefore, there is still great interest in improving the performance of earth-abundant metals for HER and OER, particularly Ni, Co, Mn, and Fe. To date, due to their relatively low stability in acids, Ni and related complexes have been rarely used as OER and HER electrocatalysts. In this work, self-supported CNF-Ni-Pd electrodes were fabricated

by combining electrospinning and ALD.[35] CNF-embedded Ni/NiO NPs were fabricated by electrospinning of PAN nanofibers loaded with nickel acetate, followed by thermal oxidation, and then pyrolysis under N_2 atmosphere. This method was developed to design CNF-Ni/NiO heterostructures with tunable composition, leading to abundant hetero-interfaces for synergy in electrocatalysis. Homogenously dispersed Ni/NiO NPs were formed on/into the CNFs. The morphology and composition of CNF-Ni/NiO could be effectively tailored by adjusting the precursor concentrations. Then, ALD was used to deposit Pd NPs around the obtained CNF-Ni/NiO electrodes, and the obtained self-supported CNF-Ni/NiO-Pd electrodes displayed high chemical stability and excellent electrocatalytic activity for HER and OER. Self-supported CNF electrodes not only enhance the electrolyte accessibility to active sites, but also increase electron transfer within the whole system. Furthermore, CNFs facilitate the dispersion of Ni/NiO and Pd NPs, hindering their agglomeration, and protect Ni/NiO NPs from oxidation and corrosion.[33] These important features of CNFs make of them a very promising electrocatalyst for HER and OER. Self-supported CNF electrodes decorated with Ni/NiO and Pd NPs exhibit excellent electrochemical activity for HER and OER with limited overpotential and small Tafel slope, and with excellent stability compared to purely self-supported CNF electrodes.

2. Experimental

2.2. Fabrication of Carbon Nanofibers with Embedded Ni/NiO NPs

Self-supported CNF mats loaded with Ni/NiO NPs were prepared by electrospinning followed by thermal peroxidation and thermal carbonization.[62] First, different amounts of nickel (II) acetate tetrahydrate were dissolved in 20 mL DMF under vigorous magnetic stirring to obtain a uniform solution. Then, 2 g of PAN powder was added to the obtained nickel acetate solution, which was then stirred for 15h to obtain the Ni-PAN precursor solution. Four solutions with different Ni

acetate contents (0%, 10%, 20%, and 50%) were prepared and loaded into 20 mL plastic syringe. The electrospinning process was performed at a distance of 10 cm (tip to collector), a voltage of 25 kV, feeding rate of 2 ml/min, and drum rotation speed of 400 rpm, respectively. The as-prepared Ni-PAN nanofibers first underwent peroxidation at 250 °C in air atmosphere for 2h, and then thermal carbonation at 1000 °C in N_2 atmosphere for 1h to obtain CNFs loaded with Ni/NiO NPs. The heating and cooling rates were kept constant at 1 °C.min^{-1}.

2.2. Atomic Layer Deposition of Pd NPs

ALD was employed to deposit Pd NPs (co-catalysts) at the surface of CNF-Ni/NiO electrodes. Pd NPs were deposited by carrying out 200 ALD cycles using a home-made ALD reactor. The ALD cycle was based on a 5s pulse of $Pd(hfac)_2$ as Pd precursor, 15s exposure, and 10s purge. This was followed by 1s pulse of formalin, exposure for 15s, and purge with Ar for 60s. The formalin container was kept at 25 °C and the bubbler containing the $Pd(hfac)_2$ precursor was heated at around 70 °C to reach the appropriate vapor pressure. The ALD lines were heated at 100 °C and the deposition chamber was set at 220 °C. This ALD process was developed and was detailed elsewhere.[63,64]

2.3. Characterization of Composite Carbon Nanofiber Electrodes

The fiber diameter and surface morphology were examined using transmission electron microscopy (TEM) (JEOL JEM 2100, Japan) and scanning electron microscopy (SEM) (Hitachi S4800, Japan) with an energy-dispersive X-ray (EDX) spectroscopy apparatus. The elemental composition was determined by elemental mapping with EDX using a Zeiss EVO HD15 microscope.

The crystal structure and crystallite size of the prepared CNF mats and Ni/NiO NPs were investigated using X-ray diffraction (XRD) (PANAlytical Xpert-PRO diffractometer) coupled with an accelerator detector (using Ni-filtered Cu radiation with a wavelength of 1.54 A).

Raman spectra (peak positions and their relative intensities) were recorded using a dispersive Raman spectrometer (Bruker, Germany, Senterra model) and a doubled Nd:YAG laser (532 nm). For X-ray photoelectron spectrometry (XPS) analysis, a Kratos Axis Ultra (Kratos Analytical, U.K.) spectrometer equipped with a monochromatic Al K_α source (1486.6 eV) was used. All spectra were recorded at a 90° take-off angle, with an analyzed area of about 0.7 x 0.3 mm. Survey spectra were acquired with 1.0 eV step and 160 eV analyzer pass energy. The high-resolution regions were acquired with 0.1 eV step (0.05 eV for O 1s and C 1s) and 20 eV pass energy. A neutralizer was used to perform the recording to compensate for the charge effects. Curves were fitted using a Gaussian/Lorentzian (70/30) peak shape after Shirley's background subtraction and using the X-vision 2.2.11 software.

Ni elemental concentration in the as-prepared CNFs was determined using atomic absorption spectroscopy (AAS) (AAnalyst 400, PerkinElmer). About 0.2 g of each CNF was annealed at 600 °C under air atmosphere for 6h and the obtained ash was dissolved in 2 mL of concentrated HNO_3 for 24 hrs. Then, the obtained solution was diluted in 200 mL of what and used to measure Ni concentration by AAS.

The average pore diameter and volume, and the specific surface area of the prepared CNFs were calculated with the Brunauer-Emmett-Teller (BET) theory from N_2 adsorption-desorption isotherms measured using the Micromeritics ASAP 2010 equipment at degassing conditions of 200 ^oC for 12h.

2.2. Electrochemical Measurements

HER and OER electrochemical tests were performed on a CHI 660E workstation using a typical three-electrode configuration. The graphitic electrode and a silver/silver chloride electrode ($E_{(RHE)} = E_{(SCE)} + 0.244\ V + 0.059 \times pH$ after calibration) were used as the counter electrode and the reference electrode, respectively. The self-supported CNF electrodes were used as the working

electrodes for HER and OER. To this aim, the as-prepared CNF electrodes were cut into circles (1 cm in diameter and 0.25 mm in thickness). The electrolyte solution was 0.5M H_2SO_4 for HER and 1M KOH for OER. Commercial Pt and IrO_2 electrodes were used as reference working electrodes for the HER and OER tests, respectively.

Cyclic voltammetry (CV) was recorded after 10 cycles using a 100 mV s^{-1} scan rate to trigger and stabilize the prepared electrodes. Linear sweep voltammetry (LSV) was recorded with a 5 mV s^{-1} scan rate for both HER and OER tests. The electrochemical impedance spectra (EIS) were measured from 10^{-1} to10^{5} Hz at a constant voltage of -0.3 V vs RHE for HER, and a voltage of 1.6 V vs RHE for OER. The electrocatalytic stability during HER was examined by determining the chronoamperometric response (i-t curves) in 0.5 M H_2SO_4 at a constant voltage of -0.3 V vs. RHE for 12h.

3. Results and Discussion

PAN has been widely used as precursor to obtain CNFs due to its high mechanical strength, good thermal stability, high carbon yield (above 65% wt/wt), and excellent electrical conductivity of the obtained CNFs. The thermal conversion of PAN nanofibers into graphitic CNFs involves oxidative stabilization, carbonization, and graphitization. The oxidative stabilization step occurs in air at 250 °C and involves the modification of the PAN nanofiber chemical structure to become more thermally stable. This will avoid their degradation during the subsequent carbonization step at 1000 °C under N_2 atmosphere. The oxidative stabilization, carbonization, and graphitization steps involve chemical reactions, such as cyclization, dehydrogenation and aromatization, oxidation and crosslinking, resulting in the formation of a fully aromatic cyclized structure.[65,66,67] In this study, self-supported CNF electrodes decorated with Ni/NiO and Pd NPs were fabricated by combining electrospinning, thermal carbonation, and ALD. The effects of the chemical composition, crystal

structure, fiber morphology, and specific surface area of the prepared CNF electrodes were investigated in view of their application for HER and OER.

3.1. Composition and Morphology of the Composite Nanofiber Electrodes

The SEM results showed that PAN thermal carbonization resulted in 3D CNF networks (**Figure 1**) that could effectively immobilize Ni/NiO and Pd NPs. The Ni acetate to PAN concentration ratio had a significant effect on the fiber diameter and morphology. The CNF fiber diameter was ~ 300 nm and it increased slightly to ~ 400 nm when Ni acetate content passed from 10% to 50%. For CNFs with the smallest (10%) Ni acetate to PAN weight ratio, the tiny Ni/NiO NPs were mainly formed within the CNFs (Figure 1 and Table 1). When the Ni to PAN weight ratio was increased to 20%, Ni/NiO NPs were formed inside and also on the surface of CNFs. The Ni/NiO NPs visible at the surface presented a rhombohedral morphology with a particle size of 55±5 nm (Figure 1). The Ni/NiO NP size distribution at the CNF surface increased to 75±5 nm and 80±8 nm with Ni acetate concentrations of 20% and 50%, respectively. SEM images also confirmed the increase of the number of Ni/NiO NPs that covered the CNF surface (Figure 1). Furthermore, SEM/EDX with elemental mapping and high-resolution was used to determine the main components of the prepared electrodes (Figure 1e). SEM/EDX analysis of C-20Ni-Pd electrode confirmed that the prepared electrodes were composed of carbon (50%), nitrogen (8%), oxygen (2%), nickel (38%) and palladium (2%). EDX element mapping was used to determine the homogenous distribution of these elements (Table 1). The edges of carbon, oxygen, nickel, palladium were well-matched with the morphology of the 3D nanofiber network structure, indicating that C, Ni, and Pd were uniformly distributed throughout the whole structure. Their uniform distribution should contribute to their electrochemical activity. AAS demonstrated that the total Ni content in the prepared electrodes was about 13% for C-10Ni, 24% for C-20Ni, and 39% for C-50Ni (Table 1).

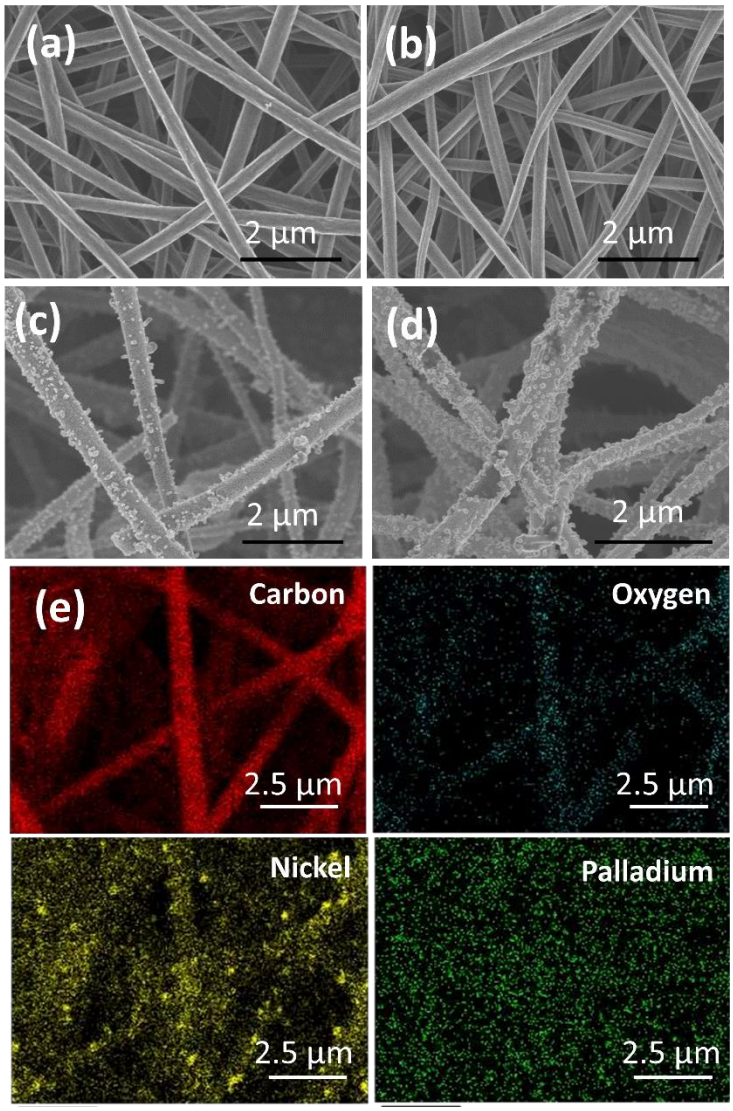

Figure 1. Field emission SEM images of the prepared CNF electrodes: (a) C-200Pd; (b) C-10Ni; (c) C-Ni20; (d) C-Ni50; and (e) Images of SEM/EDX elemental mapping of carbon, oxygen, nickel, and palladium in C-20Ni-Pd.

High-resolution TEM images of the C-20Ni electrode showed that Ni/NiO NPs can be observed as dark particles on the wire surface (Figure 2a-c). The corresponding TEM/EDX mapping analysis of the C-20Ni electrode (Figure 2d) clearly demonstrated the uniform distribution of C and Ni and the CNF surface. Their distribution was uniform, and was limited to the wire surface that was coated by Ni/NiO NPs. Moreover, high magnification high-resolution TEM images (Figure 2c) showed that Ni NPs on the CNF surface were conformally coated by graphitic layers. Figure 2 shows

the TEM images of C-20Ni-Pd of a single CNF, in which both 25±10 Ni NPs and 5±2 Pd NPs are uniformly distributed over the CNFs. TEM/EDX of C-20Ni-Pd (Figure 2d) indicated the Ni/NiO and Pd NPs and graphitic layers formed on the CNF surface had a highly crystalline structure. Ni NPs displayed a d-spacing of about 0.19±0.02 nm that corresponded to the (111) plane of the face-centered cubic (fcc) crystal structure of Ni. Pd NPs displayed a d-spacing of about 0.22±0.02 nm that corresponded to the (011) plane of the crystalline structure of Pd. Ni and Pd NPs were separated by crystalline graphitic layers with a d-spacing of about 0.33±0.02 nm. The obtained multifunctional catalyst (Pd-C-Ni nanostructure) had a heterojunction structure that allows strong electronic coupling, and can lead to higher catalytic efficiency. Gao et al.[68] fabricated CNFs-Fe_3C-Mo_2C and showed that they are efficient HER electrocatalysts leading to remarkable improvements in the HER activity compared with the single-component counterparts. This is due to their good conductivity, unique porous structure and synergistic heterojunction. Interestingly, in our work, graphene nanosheets were clearly visible on TEM images (Figure 2c). The formation of graphene nanosheets as well as Ni/NiO NPs were confirmed by Raman (Figure 3b) and XPS spectroscopy (Figure 4). They were not observed in other previously published, similar works.[69,70,71] For example, Guo et al.[70] prepared CNFs-Ni-Pd nanofibers by dissolving PAN, Pd acetate, and Ni acetate in DMF (electrospinning parameters: 100 kV m^{-1} applied voltage and 1.2 mL h^{-1} flow rate). The produced nanofibers (PAN/Ni acetate/Pd Acetate) were stabilized at 250 °C in air for 3h, reduced at 500 °C in a H_2/N_2 mixture for 2h, and then carbonized at 1000 °C.[70] In our study, the Ni acetate content was progressively increased from 10wt% to 50wt% relative to the PAN concentration. The high Ni acetate content and the electrospinning, peroxidation and carbonation parameters optimized the formation of hybrid Ni/NiO/graphene nanostructures. The produced nanofibers (CNF-20Ni) were made of a graphene architecture interpenetrated with Ni NPs grown in situ alongside the entire framework, yielding CNF-Ni/NiO interpenetrated graphene nanostructure. The CNF network structure prevents the restacking of graphene sheets and provides ample space between graphene

sheets, giving a strong structure with exceptional electrical conductivity and excellent mechanical stability.

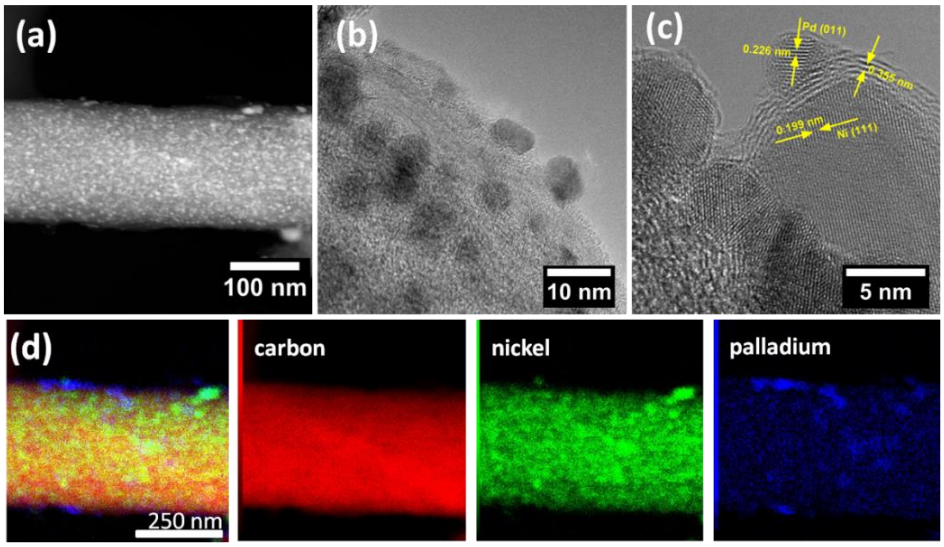

Figure 2. TEM images of the prepared nanofiber C-20Ni-Pd electrode (a) TEM image; (b, c) high magnification TEM images; and (d) EDX-based elemental mapping.

XRD measurements were performed to determine the crystal structures of the CNFs, Ni/NiO and Pd NPs (Figure 3a). All samples showed an obvious diffraction peak at ~26.4° (110) assigned to carbon (JCPDS, no. 01-089-8489). The diffraction patterns of Ni/NiO NPs embedded in CNFs were consistent with the fcc structure (JCPDS No. 04-010-6148). The peaks at ~44.3°, 51.9° and 76.5° corresponded to the (111), (220) and (200) planes of Ni metal crystals. However, formation of Ni/NiO NPs were could not be confirmed by XRD analysis but they are conformed by Raman (Figure 3b) and XPS (Figure 4) spectroscopy. The other phases (i.e. NiO and NiC) were not detected by XRD analysis. The absence of NiO and NiC could be attributed to the small content of NiO and NiC impurities, or to their amorphous nature.[75] The formation of metallic Ni crystals as a domain rather than NiO may be explained by the formation of reducing by-products, such as charcoal, activated carbon, hydrogen, during thermal carbonization under reduced pressure.[75] The average crystallite size of Ni crystals was calculated with the Scherrer equation,[72,73,74] and the obtained results were 32.0±0.4,

31.1±0.4 and 31.1±0.5 nm for C-10Ni-Pd, C-20Ni-Pd and C-50Ni-Pd, respectively (Table 1). The crystallite sizes and particle sizes were much smaller than the CNF diameter, indicating that the Ni/NiO NPs are highly dispersed in the CNFs, as observed in the TEM images (Figure 2). The diffraction peak intensity was higher for C-50Ni-Pd than for C-10Ni-Pd and C-20Ni-Pd, confirming its higher Ni/NiO NP content. A broad diffraction peak at 26.4° (002) indicated the high amorphous carbon content of pristine CNFs. Particularly, the increased intensity of the peaks at 26.4° showed that the existing Ni acetate accelerates the formation of graphitic carbon. The XRD patterns of C-0Ni-Pd did not show crystalline peaks for Pd, possibly due to the small crystallite size and number of deposited Pd NPs. In addition, as shown by SEM/EDX elemental mapping (Figure 1e), the presence of 2% oxygen in CNFs may indicate slight oxidation in CNFs or formation of NiO impurities during the peroxidation step.

To confirm the XRD results, Raman spectra of the prepared CNF-Ni/NiO-Pd electrodes were recorded to investigate the influence of Ni acetate on graphite carbon crystallinity (Figure 3b). All the prepared CNF electrodes showed an obvious D (disorder) peak at ~1364 cm^{-1} and a G (graphite) peak at ~1592 cm^{-1}. The Raman spectrum of C-50Ni-Pd also showed a strong peak at about 633 cm^{-1} that corresponds to the Ni-O bond.[76] The G peak is related to the in-plane stretching vibration of all pairs of sp2 -hybridized C atoms and does not require the presence of six-fold C atom rings of graphite. The D peak cannot be observed in perfect graphite, but only in the presence of disorders in the graphene layer structures. It represents the breathing modes of sp2 -hybridized C atoms in the rings. The relative intensities (R) of the two peaks (ID/IG) were proportional to the amount of disorder (defected carbon) in the prepared CNFs. The R value increased with the graphitized carbon transformation into amorphous carbon.[77] The ID/IG value of pure CNFs was1.18, and it decreased to 0.92 and 0.35 for C-10Ni-Pd and C-20Ni-Pd, respectively. This indicates that a graphite layer structure is gradually created with the increase of the Ni content in Ni acetate-PAN nanofibers at a specific weight ratio of Ni acetate (20%). Furthermore, the existing nickel acetate accelerated PAN

thermal transformation into graphite carbon, with a very low concentration of structural defects.[78] However, the R value of C-50Ni-Pd increased to 0.66, suggesting damage of the planar structure at higher PAN to Ni acetate weight ratios. When the Ni/NiO NP content increases from C-20Ni to C-50Ni, the amount of graphitic carbon decreases and the disordered carbonaceous structures is less able to form ordered graphitic ones. C-20Ni showed an absorption band between 2680–2730 cm^{-1}, corresponding to the first overtone of the D mode (the so-called 2D band). The presence of the 2D band is often used to confirm the existence of graphene nanosheets. The peak at 510 cm^{-1} was associated with Ni-O defects, absent in a perfect Ni-O crystal.[79]

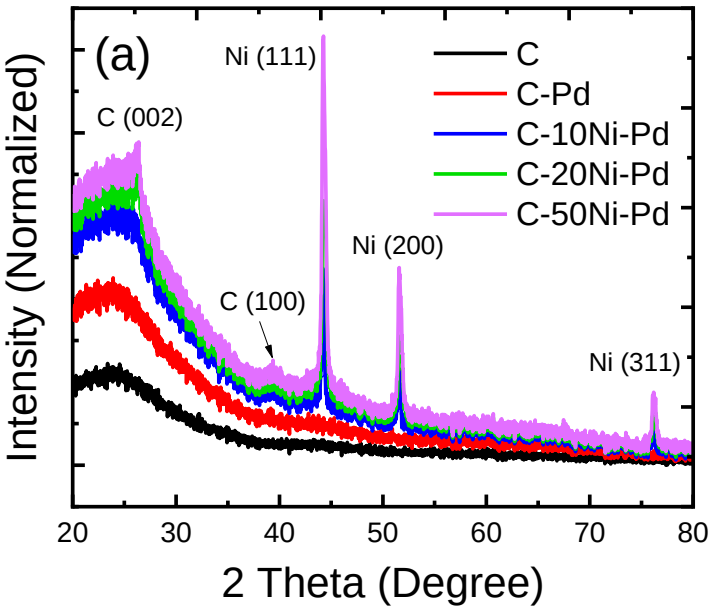

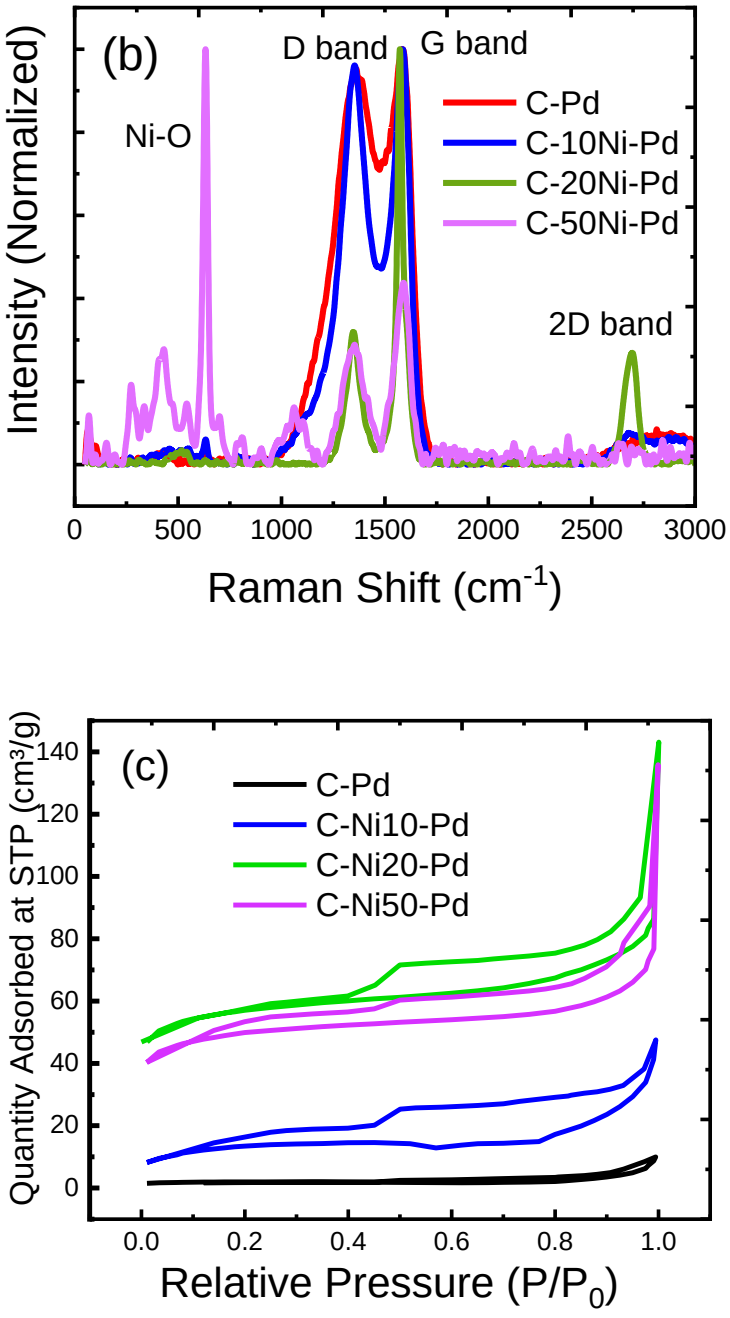

Figure 3. Characteristics of the prepared electrodes: (a) XRD patterns, (b) Raman spectra, and (c) N_2 adsorption/desorption isotherms.

The N_2 adsorption/desorption isotherms of the prepared electrodes were measured and the corresponding BET surface area and pore distribution were calculated with the Barrett–Joyner–Halenda (BJH) method (Table 1). The addition of Ni acetate to the electrospinning solution can

significantly affect the electrospinning process and the porosity of the obtained CNFs. When more Ni acetate was added to the electrospinning solution, the BET surface area significantly increased by a factor of thirty compared with pristine CNFs. It is worth noting that higher BET surface areas can significantly increase the diffusion of electrolytes, thus improving the electrochemical activity. Pure CNFs showed a microporous or non-porous structure (BET surface area: 6.7 cm^2/g and pore volume: 138.4 A°). The increased mesoporosity in C-20Ni (BET surface area: 193.9 cm^2/g and pore volume: 62.9 A°) could be attributed to the degradation products of Ni acetate during the carbonization process that act as a pore generator. The higher gas by-product evolution can cause a morphology change in the composite CNFs. The resulting increased BET surface area and decreased pore size indicated the formation of a larger mesoporous structure in the presence of Ni acetate (pore generator).

Next, XPS was performed to determine the electrode composition (i.e. C-Ni/NiO-Pd). The XPS spectra of C-20Ni and C-20Ni-Pd (Figure 4a) showed the presence of peaks corresponding to C (1s), O (2p), N (1s), and Ni (2p). This was attributed to CNF composite nature. All spectra were calibrated to the C 1s peak at 284.6 eV, which corresponds to the aliphatic chains (Figure 4b). Analysis of the C1s signal indicated the presence of four carbon species at a specific binding energy: sp^3 carbon (C-C / C-H, 284.6 eV), (C-O, 285.5 eV), (C=O, 286.8 eV), and (C-O=C, 288.2 eV) (Supplementary information, Figure S1).[80] The O 1s spectrum of C-20Ni was decomposed in three peaks located at 530.5 eV (O^{2-}, corresponds to the oxide of nickel), 532.2 eV (OH, hydroxyl and O-C), and 533.6 eV (peak of unknown origin, perhaps some residual water) (Figure 4c). The O 1s spectrum of the C-20Ni-Pd sample could not be decomposed due to charge effects. The N 1s peak of CNF and C-20Ni displayed three types of N species: C-NH, 389.7 eV, protonated nitrogen ($C\text{-}NH^+$, 401.0), and an unknown chemical bond, possibly oxidized-N (402.5 eV) (Figure 3d).[81] The 32.2 wt% of C-20Ni presented pyridinic N as the main nitrogen state. Pyridinic N is an edge-plane heteroatom, whereas graphitic N is an in-plane heteroatom of the graphene-like structure (Figure 4d and Figure

S3, Supplementary Information). The XPS spectrum of C-20Ni-Pd was characterized by Ni 2p (Figure 4e) and Pd 3d peaks (Figure 4f). This confirmed the formation of Ni and Pd NPs in CNFs. Concerning Ni oxidation state, the peak at 852.7 eV for Ni 2p3/2 indicated the existence of Ni. However, the Ni 2p3/2 (approximately 855 eV) peak could indicate the presence of some NiO impurities (Ni^{2+}).[75] This peak sharpened slightly with the increase of Ni/NiO content. The binding energy values of Ni 2p could shift towards higher values, which can be due to the transformation of the electronic structure after the deposition of Pd NPs. Therefore, these results confirm the successful deposition of Pd NPs and Ni/NiO NPs on the CNF surface. Concerning the Pd 3d spectrum of C-20Ni-Pd, the Pd 3d5/2 and Pd 3d7/2 peaks were detected at ~341.9 eV and 335.7 eV (Pd $3d_{7/2}$) (relatively weaker), the oxidation state corresponding to Pd (0). The chemical composition of the C-20Ni and C-20Ni-Pd electrodes, extracted from the XPS curves, is listed in Table S1 (Supplementary Information).

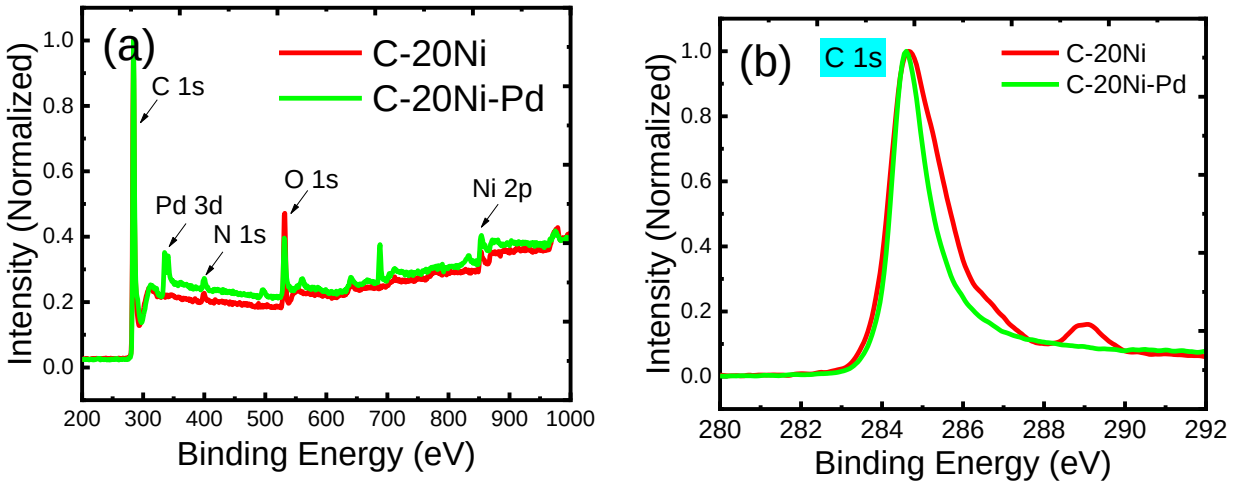

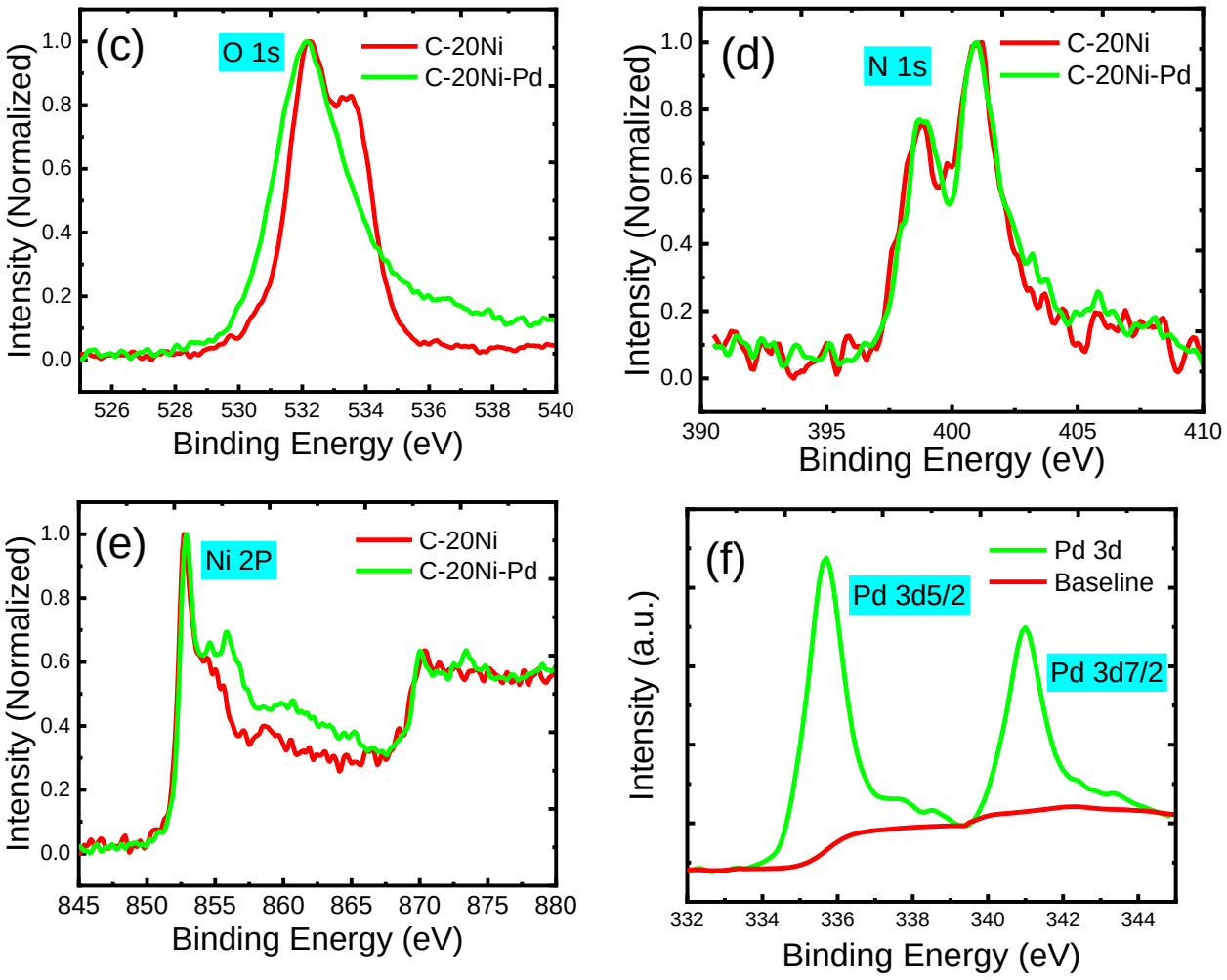

Figure 4. XPS spectra of the prepared C-20Ni and C-20Ni-Pd electrodes: (a) survey scan; (b) C 1s; (c) O 1s; (d) N 1s; (e) Ni 2P; and (f) Pd 3d.

Table 1. Characteristics of the prepared CNFs including the crystallite size calculated from the XRD data, elemental composition estimated by AAS, the ID/IG value calculated from the Raman spectra and their BET surface area, average pore diameter, and average pore volume calculated using the BJH method.

Samples	Crystallite size of Ni crystals (nm)	Elemental Composition		BET Surface Area			I_D/I_G ratio
		Carbon content (wt%)	Ni content (wt%)	BET surface area	Average pore diameter	Average pore volume	

				(cm^2/g)	(A°)	(cm^3/g)	
C	No	100	0.0	6.7	138.4	0.0143	1.18
C-10Ni	32	87	13	48.6	74.4	0.0594	0.92
C-20Ni	32	76	24	193.9	62.9	0.0716	0.35
C-50Ni	31	60	40	170.0	191.9	0.1377	0.66

3.2. Hydrogen Evolution Reactions

HER and OER tests were performed using a typical three-electrode cell. To determine the HER and OER performance of the composite CNF electrodes, the performance of commercial Pt and IrO_2 catalysts was also measured for comparison. The electrolyte solution consisted of 0.5 M H_2SO_4 for HER, and 1 M KOH for OER. As shown by the LSV curves in Figure 5a, C-20Ni-Pd was the best electrocatalyst among the tested samples, with a very limited overpotential of 63 mV at 10 mA cm^{-2} of current density, compared with C-0Ni-Pd (146 mV), C-10Ni-Pd (101 mV), and C-50Ni-Pd (167 mV). C-20Ni-Pd was in close competition with the commercial Pt catalyst (76 mV at 10 mA cm^{-2}). These data indicate that C-20Ni-Pd is the most promising catalyst for HER.

To further investigate the electrocatalytic features and HER kinetics of composite CNF electrodes, the Tafel slopes were determined using the Tafel equation and the LSV data (Figure 5b and Table S2, Supplementary Information). According to the Tafel equation ($\eta = b \log j + a$, where j is the current density, η is the overpotential and b is the Tafel slope), there are two main steps for HER in an acid medium. The first step is the primary discharge step, called "Volmer reaction" ($H_3O^+ + e^- \rightarrow H_{ads} + H_2O$, 120 mV dec^{-1}). The second step is the desorption step, called "Heyrovsky reaction" ($H_{ads} + H_3O^+ + e^- \rightarrow \mathbf{H_2}\uparrow + H_2O$, 40 mV dec^{-1}), or the recombination step, called "Tafel reaction" ($H_{ads} + H_{ads} \rightarrow \mathbf{H_2}\uparrow$, 30 mV dec^{-1}). The Tafel slope of C-20Ni-Pd (72 mV dec^{-1}) was much smaller than those of C-0Ni-Pd (79 mV dec^{-1}), C-10Ni-Pd (76 mV dec^{-1}), and C-50Ni-Pd (123 mV dec^{-1}), and was close to that of the Pt/C catalysts (36 mV dec^{-1})[37]. This implies that HER with CNF

electrodes is mainly described by the Volmer-Heyrovsky mechanism. The small Tafel slope of C-20Ni-Pd can lead to a significant increase of the current density and fastest proton discharge kinetics, correlates with efficient energy conversion, and lower η is required for HER. These are all good quality for its application as catalyst.

Water electrolysis can be performed in acidic (0.5 M H_2SO_4) or alkaline conditions (1 M KOH). In 1 M KOH, the best electrode (C-20Ni-Pd) exhibited a limited overpotential of 590 mV, reaching 10 mA cm^{-2} current density with a Tafel slope of 70 mV dec^{-1} (LSV curves in Figure 6a and Supplementary information, Figure S4). This indicates that C-20Ni-Pd is a promising electrocatalyst for HER in acidic and alkaline conditions. Water electrolysis in acidic conditions is typically employed in an electrochemical cell with a proton exchange membrane with high energy efficiency and fast H_2 evolution rate. The activity of an electrocatalyst for HER relies solely on its H-binding energy (HBE) that is sensitive to the electrolyte pH. In alkaline conditions, the electrocatalyst HBE is larger, thus resulting in slower HER reaction kinetics. However, water electrolysis in alkaline conditions may broaden the range of used electrocatalysts, from expensive rare earth elements (e.g. Pt, Ir, Ru) to earth-abundant elements (e.g. Co, Ni, Mn, Fe NPs).

The exchange current density (J_0) was calculated by extrapolation of the Tafel plot to study the electrochemical activity of the electrodes relative to the surface-active area. The J_0 of C-20Ni-Pd was about 1.15 mA cm^{-2}, which is considerably higher than the J_0 values of C-0Ni-Pd (0.86 mA cm^{-2}), C-10Ni-Pd (0.93 mA cm^{-2}), and C-50Ni-Pd (0.90 mA cm^{-2}) (Table S2, Supplementary Information). The formation of Ni/NiO NPs on the CNF surface can lead to a larger interfacial area between CNFs and Ni/NiO NPs, and higher apparent current density (compare C-20Ni-Pd and C-10Ni-Pd). However, the increase of the Ni/NiO NP content up to 50% decreased the CNF electrode electrical conductivity and increased their Ohmic resistance. The superior HER activity of C-Ni20-Pd can be attributed to the proper construction of the composite CNFs with more Ni/NiO edge sites. This can result in promising electrocatalytic activity and rapid electron transfer between CNFs and

Ni/NiO NPs, thus enhancing the electrode electrical conductivity and improving the HER performance.

To confirm this, EIS measurements were performed at a potential of -0.3 V vs RHE, and the corresponding charge transfer resistance (R_{ct}) are in Table S2, Supplementary Information. The Nyquist plots (without the Warburg impedance) for the prepared CNF electrodes are shown in **Figure 5c** fitted with the equivalent circuits (inset). According to the data extracted from the curves, the charge transfer resistance (R_{ct}) of C-20Ni-Pd (5.7 Ω) was considerably lower than that of C-0Ni-Pd (13.5 Ω), C-10Ni-Pd (15.2 Ω) and C-50Ni-Pd (23.3 Ω), as indicated in Table S2 (Supplementary Information). These results are in agreement with the high electrocatalytic activity observed with the C-20Ni-Pd electrode, as a result of the high intrinsic conductivity and excellent electrical exchange between CNFs and Ni/NiO NPs.

Then, the double-layer capacitances (Cdl) were measured to determine the electrochemical active surface areas (ECSA) of the prepared electrodes (**Figure 5d**). The CV plots of the CNF electrodes were measured in the absence of a faradic current at a potential of 60 mV vs RHE for scan rates from 20 to 200 mV s^{-1}. The Cdl and ECSA values of the prepared electrodes calculated from the CV plots are listed in Table 2. The Cdl of the C-20Ni-Pd electrode (85 mF cm^{-2}) was higher than that of C-10Ni-Pd (83 mF cm^{-2}) and C-50Ni-Pd (70 mF cm^{-2}), showing that C-20Ni-Pd has the largest catalytically active sites per surface area. This indicates that the prepared C-20Ni-Pd catalyst displays excellent electrocatalytic activity for HER.

The chemical stability of the prepared electrodes is another important characteristic to take into account when evaluating their electrochemical performance for HER. The chronoamperometry test showed that the C-20Ni-Pd electrode displayed long-term stability during 12h of water electrolysis at 60 mV (**Figure 5e)**. The XRD analysis of the C-20Ni-Pd electrode after this test (**Figure 5f**) indicated that the peak intensity corresponding to Ni crystals was slightly reduced, while

the characteristic peaks of Ni crystals showed almost no shifting, demonstrating the durability and chemical stability of this self-supported CNF electrode.

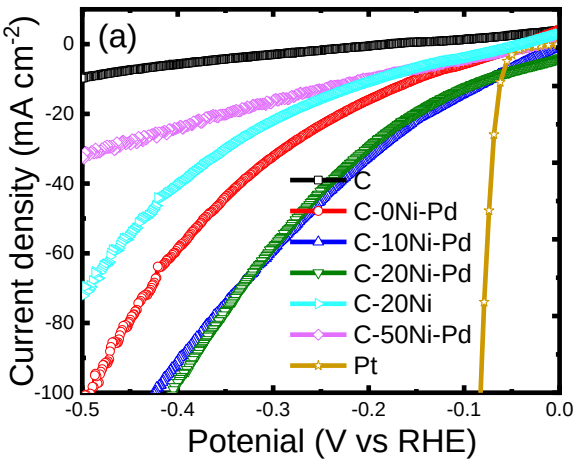

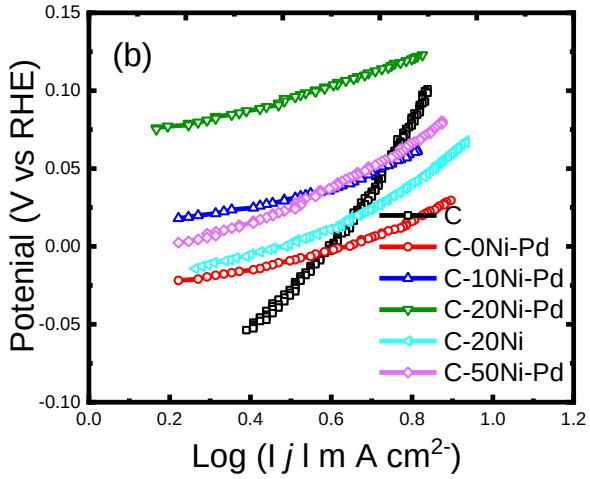

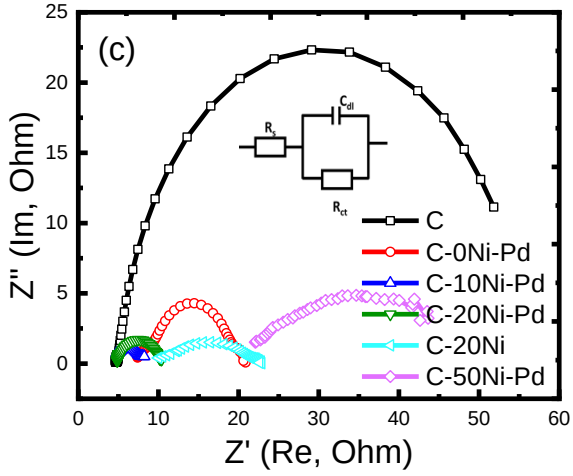

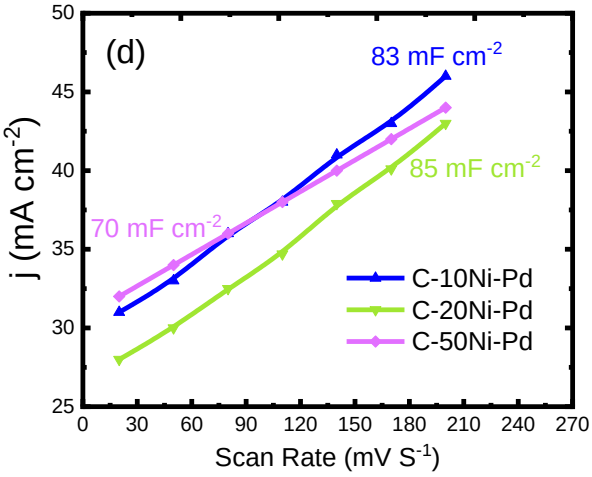

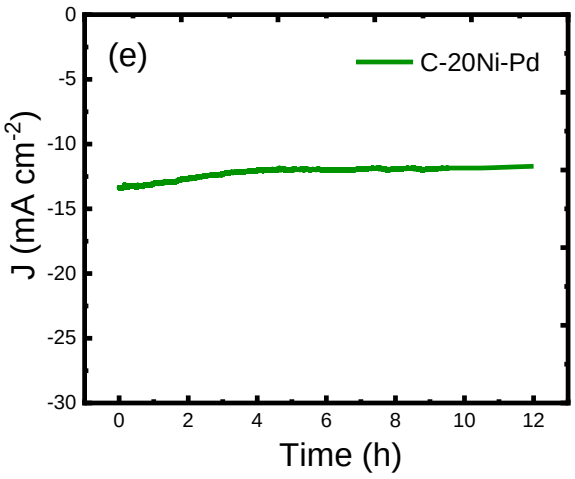

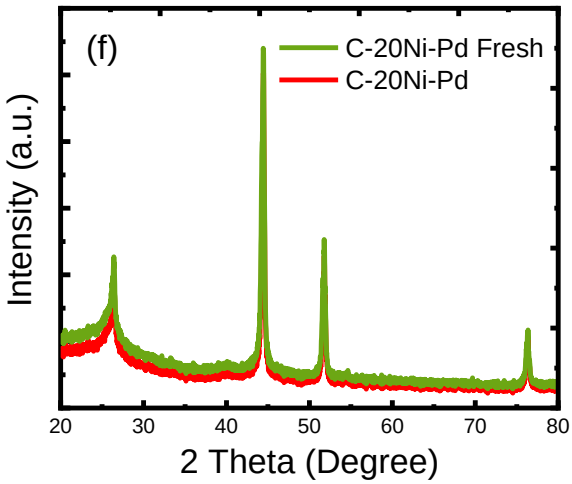

Figure 5. Electrocatalytic HER activity with the commercial Pt electrode, and the self-supported CNFs-Ni-Pd electrodes obtained in the presence of 0.5 M H_2SO_4. (a) Linear sweep voltammetry (LSV) at 5 mV s^{-1}; (b) Tafel slopes; (c) Histograms of the overpotentials measured at j =10 mA cm^{-2}; (d) The linear fit of the capacitive currents of the catalysts vs. potential scanning rates from 20 mV s^{-1} to 200 mV s^{-1}; (e) EIS at a -0.3 V potential vs RHE; inset: the Nyquist plots without the Warburg impedance for the prepared electrodes fitted with the equivalent circuits; (f) Chronoamperometric response (j-t) curve of C-20Ni-Pd at a constant voltage of 60 mV vs RHE; (g) XRD patterns of a fresh C-20Ni-Pd electrode and the electrode after the chronoamperometric response (j-t) test. Missing one panel in figure.

3.3. Oxygen Evolution Reaction

The anodic OER performance of the prepared electrodes was studied by testing their OER electrocatalytic activities in an electrolyte solution of 1 M KOH. The tests showed that C-10Ni-Pd displayed outstanding OER activity with a relatively lower overpotential of approximately 1.61 mV to reach 10 mA cm^{-2} compared with the commercial IrO_2 electrode (1.68 mV) (Figure 6a). The Tafel slopes (Figure 6b and Table 3), calculated as before, of C-10Ni-Pd (272 mV dec^{-1}) and C-20Ni-Pd (280 mV dec^{-1}) were much smaller than those of C-0Ni-Pd (358 mV dec^{-1}) and C-50Ni-Pd (419 mV dec^{-1}). This suggested that the C-10Ni-Pd electrode possesses the highest catalytic activity for OER due to the unique porous architecture of the nanofiber composite and the conductivity boost thanks to the Ni edge on the outer surface of CNFs, as revealed by EDX elemental mapping (Figure 2d).[37] The J_0 value of C-10Ni-Pd was about 22.4 mA cm^{-2}, which is relatively higher than that of C-0Ni-Pd (21.40 mA cm^{-2}), C-20Ni-Pd (20.89 mA cm^{-2}), and C-50Ni-Pd (15.74 mA cm^{-2}) (Table 3). EIS measurements were performed at a potential of 1.6 V vs RHE and the corresponding charge transfer resistance (R_{ct}) values are listed in Table 3. The charge transfer resistance (R_{ct}) of C-20Ni-Pd (2.2 Ω)

was considerably lower than that of C-0Ni-Pd (7.9 Ω), C-10Ni-Pd (3.0 Ω) and C-50Ni-Pd (5.4 Ω) (Figure 6c). These results confirmed the high electrocatalytic activity of the C-20Ni-Pd electrode and the excellent electrical exchange between CNFs and Ni/NiO NPs.

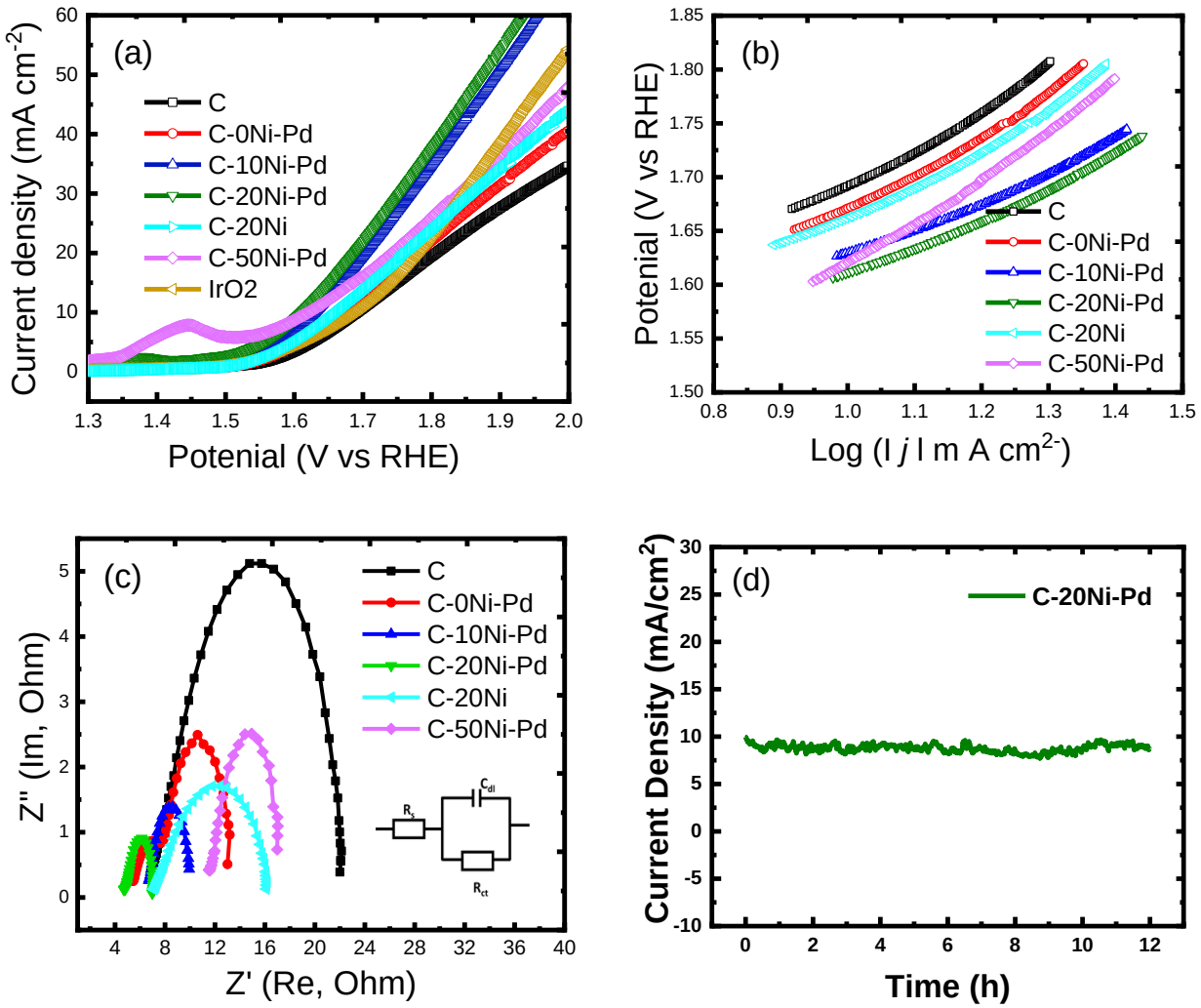

Figure 6. Electrocatalytic activity of OER with the commercial IrO_2 electrode, and the self-supported CNFs-Ni-Pd electrodes measured in the presence of 1 M KOH. (a) Linear sweep voltammetry of the different samples; (b) Tafel slopes; (c) EIS at the potential of 1.6 V vs RHE. The inset shows the Nyquist plots without the Warburg impedance for the prepared electrodes fitted with the equivalent circuits; (d) Chronoamperometric response (j-t) curve of C-20Ni-Pd at 1.6V vs RHE.

The best electrode (C-20Ni-Pd) displayed optimal HER and OER activity with a lower overpotential at 10 mA cm^{-2} current density and also a smaller Tafel slope, which is better than what

reported for recently described electrocatalysts.[23,37,29,82] For example, Chen et al.[37] prepared CNFs loaded with Pd and Ni using $PdCl_2$ and $NiN_2O_6 \cdot 6H_2O$ with a weight ratio of 1:2. The prepared electrodes exhibited high HER with a limited overpotential of 55 mV at 10 mA cm^{-2} current density in 0.5 M H_2SO_4. Conversely, in the present work, a very small amount of Pd NPs was used compared with what reported in the literature (Supplementary information, Table S3). The outstanding electrocatalytic activity of C-20Ni-Pd in water splitting can be attributed to (i) the high loading percentage of Ni/NiO NPs in CNFs; (ii) the formation of Ni/NiO NPs inside and on the surface of CNFs; (iii) the deposition by ALD of ~5 Pd NPs on the surface of the CNFs and Ni/NiO NPs alter the electronic structures and lead to enhanced electrical conductivity, rapid charge transfer, and higher electrochemical activity; (iv) the ultrathin protective layer of Pd NPs over the composite CNFs and the embedded Pd NPs might improve the chemical stability; (v) the protection of an inert layer of graphitic carbon and Pd NPs over the Ni/NiO NPs surface might prevent the surface and structural decomposition of the prepared CNFs-Ni/NiO; (vi) Pd NP deposition on the Ni/NiO NP surface improves the CNF corrosion resistance and electrochemical stability; (vii) the CNF network structure facilitates the diffusion of the gas and electrolyte during electrolysis; and (viii) heterostructures composed of different active materials with various H-binding energy (i.e. CNF-Ni/NiO-Pd) offer a superior HER activity compared with their counterparts (i.e. CNF-Ni/NiO and CNF-Pd nanofibers). This is explained by the well-exposed active sites or by the optimized electronic configuration on the interfaces.[83] The strong H binding on the heterostructures (CNF-Ni/NiO-Pd) and the relatively weak binding on C-Ni or C-Pd might explain why CNF-Ni/NiO-Pd heterostructures can efficiently catalyze both H^+ reduction and H_{ads} desorption in HER, resulting in optimized HER kinetics and superior activity.[68]

Conclusion

In summary, efficient, highly conductive and self-supported CNF-Ni/NiO-Pd electrodes with heterostructure have been successfully fabricated by combining electrospinning, thermal treatment, and ALD. Self-supported CNFs mats embedded with Ni/NiO NPs were fabricated by electrospinning a PAN solution containing Ni acetate followed by peroxidation under air, and then thermal carbonization under nitrogen atmosphere. The self-supported CNFs mats were further modified with Pd NPs using the ALD method, and then the unmodified and modified mats were tested as electrodes for HER and OER in acidic and alkaline solution, respectively. The self-supported CNF electrodes decorated with Ni/NiO and Pd NPs displayed high HER and OER activity and excellent stability, compared with the commercial Pt and IrO_2 catalysts. The morphology and composition of the composite CNFs were controlled by adjusting the precursor nanofibers. The composite CNF electrodes showed excellent electrochemical activity, low overpotential, remarkable exchange current density and long-term stability compared with pristine CNFs. The control of the CNF diameter, as well as the size and dispersion of Ni/NiO and Pd NPs on CNFs explain their high HER and OER activity. The C-20Ni-Pd electrode, which has very high Ni NPs content (up to 50%) with traces of NiO, and small Pd NPs, acts as remarkable electrocatalyst for HER and OER. Its outstanding electrocatalytic activity can be attributed to the positive and synergistic effect between the CNFs, Ni/NiO and Pd NPs at the nanoscale interfaces. The fast kinetics observed for gas desorption might originate from the CNF network structure. The present study describes a new strategy for the design of self-supported CNF electrodes for energy conversion-related applications. Self-supported CNF electrodes loaded with Ni/NiO and Pd NPs can be considered as promising candidates for large-scale HER and OER applications at the place of Pt and IrO_2 electrodes. The approach developed in this work is highly versatile and is applicable for the in situ synthesis of CNFs that incorporate other transition metals and metal alloys (e.g. Ni, Mn, Co, Fe, Mo) for application in water electrolysis and electrochemical oxidation of wastewater. ALD deposition of tiny metal NPs

(e.g. Pd, Au, Ag) of different thickness also is highly versatile and is applicable for water electrolysis and electrochemical oxidation of wastewater.

Conflict of interest

All authors have declared that there is no conflict of interest regarding the contributions in this publication.

Acknowledgments

Very special thanks to the Egypt-France Joint Program (STDF-IFE 2019, Project No. 31216) for giving Dr. Ahmed Barhoum (Lecturer of Nanotechnology at Helwan University and Project PI for the Egyptian Side) the opportunity and financial support to pursue a research stay at the Institut Européen des Membranes (IEM), Université de Montpellier. I.I. acknowledges the partial financial support by project H2020-MSCA-RISE-2017, 'CanBioSe' (Project number: 778157).

References

(1) Roger, I.; Shipman, M. A.; Symes, M. D. Earth-Abundant Catalysts for Electrochemical and Photoelectrochemical Water Splitting. *Nat. Rev. Chem.* **2017**, *1* (1), 0003. https://doi.org/10.1038/s41570-016-0003.

(2) Shalan, A. E.; Barhoum, A.; Elseman, A. M.; Rashad, M. M.; Lira-Cantú, M. Nanofibers as Promising Materials for New Generations of Solar Cells. In *Handbook of Nanofibers*; Springer International Publishing: Cham, 2018; pp 1–33. https://doi.org/10.1007/978-3-319-42789-8_51-1.

(3) Peter, L. M. Photoelectrochemical Water Splitting. A Status Assessment. *Electroanalysis* **2015**, *27* (4), 864–871. https://doi.org/10.1002/elan.201400587.

(4) El-maghrabi, H. H.; Barhoum, A.; Nada, A. A.; Mohamed, Y.; Mikhail, S.; Youssef, A. M. Synthesis of Mesoporous Core-Shell CdS@TiO2 (0D and 1D) Photocatalysts for Solar-Driven

Hydrogen Fuel Production. *"Journal Photochem. Photobiol. A Chem.* **2018**, *351*, 261–270. https://doi.org/10.1016/j.jphotochem.2017.10.048.

(5) Pavlenko, M.; Siuzdak, K.; Coy, E.; Jancelewicz, M.; Jurga, S.; Iatsunskyi, I. Silicon/TiO2 Core-Shell Nanopillar Photoanodes for Enhanced Photoelectrochemical Water Oxidation. *Int. J. Hydrogen Energy* **2017**, *42* (51), 30076–30085. https://doi.org/10.1016/j.ijhydene.2017.10.033.

(6) Zhou, T.; Xu, W.; Zhang, N.; Du, Z.; Zhong, C.; Yan, W.; Ju, H.; Chu, W.; Jiang, H.; Wu, C.; et al. Ultrathin Cobalt Oxide Layers as Electrocatalysts for High-Performance Flexible Zn–Air Batteries. *Adv. Mater.* **2019**, *31* (15), 1807468. https://doi.org/10.1002/adma.201807468.

(7) Zhao, Y.; Zhang, J.; Li, K.; Ao, Z.; Wang, C.; Liu, H.; Sun, K.; Wang, G. Electrospun Cobalt Embedded Porous Nitrogen Doped Carbon Nanofibers as an Efficient Catalyst for Water Splitting. *J. Mater. Chem. A* **2016**, *4* (33), 12818–12824. https://doi.org/10.1039/C6TA04244A.

(8) McCrory, C. C. L.; Jung, S.; Ferrer, I. M.; Chatman, S. M.; Peters, J. C.; Jaramillo, T. F. Benchmarking Hydrogen Evolving Reaction and Oxygen Evolving Reaction Electrocatalysts for Solar Water Splitting Devices. *J. Am. Chem. Soc.* **2015**, *137* (13), 4347–4357. https://doi.org/10.1021/ja510442p.

(9) Wang, Y.; Zhang, G.; Xu, W.; Wan, P.; Lu, Z.; Li, Y.; Sun, X. A 3D Nanoporous Ni-Mo Electrocatalyst with Negligible Overpotential for Alkaline Hydrogen Evolution. *ChemElectroChem* **2014**, *1* (7), 1138–1144. https://doi.org/10.1002/celc.201402089.

(10) Kawashima, A.; Akiyama, E.; Habazaki, H.; Hashimoto, K. Characterization of Sputter-Deposited Ni-Mo and Ni-W Alloy Electrocatalysts for Hydrogen Evolution in Alkaline Solution. *Mater. Sci. Eng. A* **1997**, *226–228*, 905–909. https://doi.org/10.1016/S0921-5093(97)80095-0.

(11) Li, S.; Wang, Y.; Peng, S.; Zhang, L.; Al-Enizi, A. M.; Zhang, H.; Sun, X.; Zheng, G. Co-Ni-

Based Nanotubes/Nanosheets as Efficient Water Splitting Electrocatalysts. *Adv. Energy Mater.* **2016**, *6* (3), 1501661. https://doi.org/10.1002/aenm.201501661.

(12) Han, L.; Dong, S.; Wang, E. Transition-Metal (Co, Ni, and Fe)-Based Electrocatalysts for the Water Oxidation Reaction. *Adv. Mater.* **2016**, *28* (42), 9266–9291. https://doi.org/10.1002/adma.201602270.

(13) Navarro-Flores, E.; Chong, Z.; Omanovic, S. Characterization of Ni, NiMo, NiW and NiFe Electroactive Coatings as Electrocatalysts for Hydrogen Evolution in an Acidic Medium. *J. Mol. Catal. A Chem.* **2005**, *226* (2), 179–197. https://doi.org/10.1016/J.MOLCATA.2004.10.029.

(14) Barhoum, A.; Shalan, A. E.; El-Hout, S. I.; Ali, G. A. M.; Abdelbasir, S. M.; Abu Serea, E. S.; Ibrahim, A. H.; Pal, K. A Broad Family of Carbon Nanomaterials: Classification, Properties, Synthesis, and Emerging Applications. In *Handbook of Nanofibers*; Springer International Publishing, 2019; pp 1–40. https://doi.org/10.1007/978-3-319-42789-8_59-1.

(15) Sudha, P. N.; Sangeetha, K.; Vijayalakshmi, K.; Barhoum, A. Nanomaterials History, Classification, Unique Properties, Production and Market. In *Emerging Applications of Nanoparticles and Architectural Nanostructures: Current Prospects and Future Trends*; Elsevier Inc., 2018; pp 341–384. https://doi.org/10.1016/B978-0-323-51254-1.00012-9.

(16) Barhoum, A.; Samyn, P.; Öhlund, T.; Dufresne, A. Review of Recent Research on Flexible Multifunctional Nanopapers. *Nanoscale* **2017**, *9* (40), 15181–15205. https://doi.org/10.1039/c7nr04656a.

(17) Nnaji, C. O.; Jeevanandam, J.; Chan, Y. S.; Danquah, M. K.; Pan, S.; Barhoum, A. Engineered Nanomaterials for Wastewater Treatment: Current and Future Trends. In *Fundamentals of Nanoparticles*; Elsevier, 2018; pp 129–168. https://doi.org/10.1016/b978-0-323-51255-8.00006-9.

(18) Coy, E.; Yate, L.; Valencia, D. P.; Aperador, W.; Siuzdak, K.; Torruella, P.; Azanza, E.;

Estrade, S.; Iatsunskyi, I.; Peiro, F.; et al. High Electrocatalytic Response of a Mechanically Enhanced NbC Nanocomposite Electrode Toward Hydrogen Evolution Reaction. *ACS Appl. Mater. Interfaces* **2017**, *9* (36), 30872–30879. https://doi.org/10.1021/acsami.7b10317.

(19) Valencia, D. P.; Yate, L.; Aperador, W.; Li, Y.; Coy, E. High Electrocatalytic Response of Ultra-Refractory Ternary Alloys of Ta-Hf-C Carbide toward Hydrogen Evolution Reaction in Acidic Media. *J. Phys. Chem. C* **2018**, *122* (44), 25433–25440. https://doi.org/10.1021/acs.jpcc.8b08123.

(20) Hammani, S.; Barhoum, A.; Nagarajan, S.; Bechelany, M. Toner Waste Powder (TWP) as a Filler for Polymer Blends (LDPE/HIPS) for Enhanced Electrical Conductivity. *Materials (Basel).* **2019**, *12* (19), 3062. https://doi.org/10.3390/ma12193062.

(21) Abdel-Haleem, F. M.; Salah, A.; Rizk, M. S.; Moustafa, H.; Bechelany, M.; Barhoum, A. Carbon-based Nanosensors for Salicylate Determination in Pharmaceutical Preparations. *Electroanalysis* **2019**, *31* (4), 778–789. https://doi.org/10.1002/elan.201800728.

(22) Ali, A.; Akyüz, D.; Asghar, M. A.; Koca, A.; Keskin, B. Free-Standing Carbon Nanotubes as Non-Metal Electrocatalyst for Oxygen Evolution Reaction in Water Splitting. *Int. J. Hydrogen Energy* **2018**, *43* (2), 1123–1128. https://doi.org/10.1016/J.IJHYDENE.2017.11.060.

(23) Wu, Z.-Y.; Ji, W.-B.; Hu, B.-C.; Liang, H.-W.; Xu, X.-X.; Yu, Z.-L.; Li, B.-Y.; Yu, S.-H. Partially Oxidized Ni Nanoparticles Supported on Ni-N Co-Doped Carbon Nanofibers as Bifunctional Electrocatalysts for Overall Water Splitting. *Nano Energy* **2018**, *51*, 286–293. https://doi.org/10.1016/J.NANOEN.2018.06.071.

(24) Hu, Q.; Li, G.; Li, G.; Liu, X.; Zhu, B.; Chai, X.; Zhang, Q.; Liu, J.; He, C. Trifunctional Electrocatalysis on Dual-Doped Graphene Nanorings–Integrated Boxes for Efficient Water Splitting and Zn–Air Batteries. *Adv. Energy Mater.* **2019**, *9* (14), 1803867. https://doi.org/10.1002/aenm.201803867.

(25) El-maghrabi, H. H.; Ahmed, E.; Soliman, F. S.; Mohamed, Y.; Amin, A. E. One Pot

Environmental Friendly Nanocomposite Synthesis of Novel TiO_2 -Nanotubes on Graphene Sheets as Effective Photocatalyst. *Egypt. J. Pet.* **2016**, *25* (4), 575–584. https://doi.org/10.1016/j.ejpe.2015.12.004.

(26) Wang, J.; Zhu, H.; Yu, D.; Chen, J.; Chen, J.; Zhang, M.; Wang, L.; Du, M. Engineering the Composition and Structure of Bimetallic Au–Cu Alloy Nanoparticles in Carbon Nanofibers: Self-Supported Electrode Materials for Electrocatalytic Water Splitting. *ACS Appl. Mater. Interfaces* **2017**, *9* (23), 19756–19765. https://doi.org/10.1021/acsami.7b01418.

(27) Wang, J.; Zhu, H.; Chen, J.; Zhang, B.; Zhang, M.; Wang, L.; Du, M. Small and Well-Dispersed Cu Nanoparticles on Carbon Nanofibers: Self-Supported Electrode Materials for Efficient Hydrogen Evolution Reaction. *Int. J. Hydrogen Energy* **2016**, *41* (40), 18044–18049. https://doi.org/10.1016/J.IJHYDENE.2016.08.058.

(28) Li, M.; Zhu, Y.; Wang, H.; Wang, C.; Pinna, N.; Lu, X. Ni Strongly Coupled with Mo_2C Encapsulated in Nitrogen-Doped Carbon Nanofibers as Robust Bifunctional Catalyst for Overall Water Splitting. *Adv. Energy Mater.* **2019**, *9* (10), 1803185. https://doi.org/10.1002/aenm.201803185.

(29) Ding, Q.; Liu, M.; Miao, Y.-E.; Huang, Y.; Liu, T. Electrospun Nickel-Decorated Carbon Nanofiber Membranes as Efficient Electrocatalysts for Hydrogen Evolution Reaction. *Electrochim. Acta* **2015**, *159*, 1–7. https://doi.org/10.1016/J.ELECTACTA.2015.01.197.

(30) Chen, X.; Cheng, L.; Li, H.; Barhoum, A.; Zhang, Y.; He, X.; Yang, W.; Bubakir, M. M.; Chen, H. Magnetic Nanofibers: Unique Properties, Fabrication Techniques, and Emerging Applications. *ChemistrySelect* **2018**, *3* (31), 9127–9143. https://doi.org/10.1002/slct.201702480.

(31) Rasouli, R.; Barhoum, A.; Bechelany, M.; Dufresne, A. Nanofibers for Biomedical and Healthcare Applications. *Macromol. Biosci.* **2019**, *19* (2), 1800256. https://doi.org/10.1002/mabi.201800256.

(32) Abdel-Haleem, F. M.; Saad, M.; Barhoum, A.; Bechelany, M.; Rizk, M. S. PVC Membrane, Coated-Wire, and Carbon-Paste Ion-Selective Electrodes for Potentiometric Determination of Galantamine Hydrobromide in Physiological Fluids. *Mater. Sci. Eng. C* **2018**, *89*, 140–148. https://doi.org/10.1016/J.MSEC.2018.04.001.

(33) Haichao, L.; Haoyi, L.; Bubakir, M. M.; Weimin, Y.; Barhoum, A. Engineering Nanofibers as Electrode and Membrane Materials for Batteries, Supercapacitors, and Fuel Cells. In *Handbook of Nanofibers*; Springer International Publishing: Cham, 2018; pp 1–27. https://doi.org/10.1007/978-3-319-42789-8_52-1.

(34) Barhoum, A.; Pal, K.; Rahier, H.; Uludag, H.; Kim, I. S.; Bechelany, M. Nanofibers as New-Generation Materials: From Spinning and Nano-Spinning Fabrication Techniques to Emerging Applications. *Appl. Mater. Today* **2019**, *17*, 1–35. https://doi.org/10.1016/j.apmt.2019.06.015.

(35) Gugulothu, D.; Barhoum, A.; Nerella, R.; Ajmer, R.; Bechlany, M. Fabrication of Nanofibers: Electrospinning and Non-Electrospinning Techniques. In *Handbook of Nanofibers*; Springer International Publishing: Cham, 2018; pp 1–34. https://doi.org/10.1007/978-3-319-42789-8_6-2.

(36) Prasad, S.; Kumar, V.; Kirubanandam, S.; Barhoum, A. Engineered Nanomaterials: Nanofabrication and Surface Functionalization. In *Emerging Applications of Nanoparticles and Architectural Nanostructures: Current Prospects and Future Trends*; Elsevier Inc., 2018; pp 305–340. https://doi.org/10.1016/B978-0-323-51254-1.00011-7.

(37) Chen, J.; Chen, J.; Yu, D.; Zhang, M.; Zhu, H.; Du, M. Carbon Nanofiber-Supported PdNi Alloy Nanoparticles as Highly Efficient Bifunctional Catalysts for Hydrogen and Oxygen Evolution Reactions. *Electrochim. Acta* **2017**, *246*, 17–26. https://doi.org/10.1016/J.ELECTACTA.2017.06.047.

(38) Karatutlu, A.; Barhoum, A.; Sapelkin, A. Theories of Nanoparticle and Nanostructure

Formation in Liquid Phase. In *Emerging Applications of Nanoparticles and Architectural Nanostructures: Current Prospects and Future Trends*; Elsevier Inc., 2018; pp 597–619. https://doi.org/10.1016/B978-0-323-51254-1.00020-8.

(39) Gopalakrishnan, R.; Li, Y.; Smekens, J.; Barhoum, A.; Van Assche, G.; Omar, N.; Van Mierlo, J. Electrochemical Impedance Spectroscopy Characterization and Parameterization of Lithium Nickel Manganese Cobalt Oxide Pouch Cells: Dependency Analysis of Temperature and State of Charge. *Ionics (Kiel).* **2019**, *25* (1), 111–123. https://doi.org/10.1007/s11581-018-2595-2.

(40) Motoyama, Y.; Hosokawa, S. Carbon Nanofibers as Supports for Metal Nanoparticles. *Carbon N. Y.* **2015**, *87*, 463. https://doi.org/10.1016/j.carbon.2015.02.033.

(41) Cremers, V.; Rampelberg, G.; Barhoum, A.; Walters, P.; Claes, N.; Oliveira, T. M. D.; Assche, G. V.; Bals, S.; Dendooven, J.; Detavernier, C. Oxidation Barrier of Cu and Fe Powder by Atomic Layer Deposition. *Surf. Coatings Technol.* **2018**, *349*. https://doi.org/10.1016/j.surfcoat.2018.06.048.

(42) Weber, M. J.; Verheijen, M. A.; Bol, A. A.; Kessels, W. M. M. Sub-Nanometer Dimensions Control of Core/Shell Nanoparticles Prepared by Atomic Layer Deposition. *Nanotechnology* **2015**, *26* (9). https://doi.org/10.1088/0957-4484/26/9/094002.

(43) Graniel, O.; Weber, M.; Balme, S.; Miele, P.; Bechelany, M. Atomic Layer Deposition for Biosensing Applications. *Biosensors and Bioelectronics*. Elsevier Ltd December 2018, pp 147–159. https://doi.org/10.1016/j.bios.2018.09.038.

(44) Weber, M.; Julbe, A.; Ayral, A.; Miele, P.; Bechelany, M. Atomic Layer Deposition for Membranes: Basics, Challenges, and Opportunities. *Chem. Mater.* **2018**, *30* (21), 7368–7390. https://doi.org/10.1021/acs.chemmater.8b02687.

(45) Weber, M.; Koonkaew, B.; Balme, S.; Utke, I.; Picaud, F.; Iatsunskyi, I.; Coy, E.; Miele, P.; Bechelany, M. Boron Nitride Nanoporous Membranes with High Surface Charge by Atomic

Layer Deposition. *ACS Appl. Mater. Interfaces* **2017**, *9* (19), 16669–16678. https://doi.org/10.1021/acsami.7b02883.

(46) Van Delft, J. A.; Garcia-Alonso, D.; Kessels, W. M. M. Atomic Layer Deposition for Photovoltaics: Applications and Prospects for Solar Cell Manufacturing. *Semicond. Sci. Technol.* **2012**, *27* (7). https://doi.org/10.1088/0268-1242/27/7/074002.

(47) Leskelä, M.; Ritala, M. Atomic Layer Deposition (ALD): From Precursors to Thin Film Structures. In *Thin Solid Films*; 2002; Vol. 409, pp 138–146. https://doi.org/10.1016/S0040-6090(02)00117-7.

(48) Kertmen, A.; Barbé, E.; Szkoda, M.; Siuzdak, K.; Babačić, V.; Torruella, P.; Iatsunskyi, I.; Kotkowiak, M.; Rytel, K.; Estradé, S.; et al. Photoelectrochemically Active N-Adsorbing Ultrathin TiO 2 Layers for Water-Splitting Applications Prepared by Pyrolysis of Oleic Acid on Iron Oxide Nanoparticle Surfaces under Nitrogen Environment. *Adv. Mater. Interfaces* **2019**, *6* (3). https://doi.org/10.1002/admi.201801286.

(49) George, S. M. Atomic Layer Deposition: An Overview. *Chem. Rev.* **2010**, *110* (1), 111–131. https://doi.org/10.1021/cr900056b.

(50) Johnson, R. W.; Hultqvist, A.; Bent, S. F. A Brief Review of Atomic Layer Deposition: From Fundamentals to Applications. *Mater. Today* **2014**, *17* (5), 236–246. https://doi.org/10.1016/J.MATTOD.2014.04.026.

(51) Celebioglu, A.; Ranjith, K. S.; Eren, H.; Biyikli, N.; Uyar, T. Surface Decoration of Pt Nanoparticles via ALD with TiO2 Protective Layer on Polymeric Nanofibers as Flexible and Reusable Heterogeneous Nanocatalysts. *Sci. Rep.* **2017**, *7* (1), 13401. https://doi.org/10.1038/s41598-017-13805-2.

(52) Mackus, A. J. M.; Weber, M. J.; Thissen, N. F. W.; Garcia-Alonso, D.; Vervuurt, R. H. J.; Assali, S.; Bol, A. A.; Verheijen, M. A.; Kessels, W. M. M. Atomic Layer Deposition of Pd and Pt Nanoparticles for Catalysis: On the Mechanisms of Nanoparticle Formation.

Nanotechnology **2015**, *27* (3). https://doi.org/10.1088/0957-4484/27/3/034001.

(53) Lu, J.; Low, K.-B.; Lei, Y.; Libera, J. A.; Nicholls, A.; Stair, P. C.; Elam, J. W. Toward Atomically-Precise Synthesis of Supported Bimetallic Nanoparticles Using Atomic Layer Deposition. *Nat. Commun.* **2014**, *5* (1), 3264. https://doi.org/10.1038/ncomms4264.

(54) Cao, K.; Zhu, Q.; Shan, B.; Chen, R. Controlled Synthesis of Pd/Pt Core Shell Nanoparticles Using Area-Selective Atomic Layer Deposition. *Sci. Rep.* **2015**, *5* (1), 8470. https://doi.org/10.1038/srep08470.

(55) Weber, M. J.; MacKus, A. J. M.; Verheijen, M. A.; Van Der Marel, C.; Kessels, W. M. M. Supported Core/Shell Bimetallic Nanoparticles Synthesis by Atomic Layer Deposition. *Chem. Mater.* **2012**, *24* (15), 2973–2977. https://doi.org/10.1021/cm301206e.

(56) Cheng, N.; Liu, J.; Sun, X. Electrocatalysts by Atomic Layer Deposition for Fuel Cell Applications. *Nano Energy* **2016**, *29*, 220–242. https://doi.org/10.1016/J.NANOEN.2016.01.016.

(57) Liu, L. Atomic Layer Deposition of Electrocatalysts for Use in Fuel Cells and Electrolyzers. In *Atomic Layer Deposition in Energy Conversion Applications*; Wiley-VCH Verlag GmbH & Co. KGaA: Weinheim, Germany, 2017; pp 149–181. https://doi.org/10.1002/9783527694822.ch5.

(58) Song, Z.; Banis, M. N.; Zhang, L.; Wang, B.; Yang, L.; Banham, D.; Zhao, Y.; Liang, J.; Zheng, M.; Li, R.; et al. Origin of Achieving the Enhanced Activity and Stability of Pt Electrocatalysts with Strong Metal-Support Interactions via Atomic Layer Deposition. *Nano Energy* **2018**, *53*, 716–725. https://doi.org/10.1016/J.NANOEN.2018.09.008.

(59) Anitha, V. C.; Zazpe, R.; Krbal, M.; Yoo, J.; Sopha, H.; Prikryl, J.; Cha, G.; Slang, S.; Schmuki, P.; Macak, J. M. Anodic TiO2 Nanotubes Decorated by Pt Nanoparticles Using ALD: An Efficient Electrocatalyst for Methanol Oxidation. *J. Catal.* **2018**, *365*, 86–93. https://doi.org/10.1016/J.JCAT.2018.06.017.

(60) Young, K. M. H.; Hamann, T. W. Enhanced Photocatalytic Water Oxidation Efficiency with Ni(OH) 2 Catalysts Deposited on α-Fe 2 O 3 via ALD. *Chem. Commun.* **2014**, *50* (63), 8727. https://doi.org/10.1039/C4CC02598A.

(61) Guterman, V. E.; Belenov, S. V.; Alekseenko, A. A.; Lin, R.; Tabachkova, N. Y.; Safronenko, O. I. Activity and Stability of Pt/C and Pt-Cu/C Electrocatalysts. *Electrocatalysis* **2018**, *9* (5), 550–562. https://doi.org/10.1007/s12678-017-0451-1.

(62) Barhoum, A.; Rasouli, R.; Yousefzadeh, M.; Rahier, H.; Bechelany, M. Nanofiber Technology: History and Developments. In *Handbook of Nanofibers*; Springer International Publishing: Cham, 2018; pp 1–42. https://doi.org/10.1007/978-3-319-42789-8_54-1.

(63) Merenda, A.; Weber, M.; Bechelany, M.; Allioux, F. M.; Hyde, L.; Kong, L.; Dumée, L. F. Fabrication of Pd-TiO 2 Nanotube Photoactive Junctions via Atomic Layer Deposition for Persistent Pesticide Pollutants Degradation. *Appl. Surf. Sci.* **2019**, *483*, 219–230. https://doi.org/10.1016/j.apsusc.2019.03.285.

(64) Weber, M.; Collot, P.; El Gaddari, H.; Tingry, S.; Bechelany, M.; Holade, Y. Enhanced Catalytic Glycerol Oxidation Activity Enabled by Activated-Carbon-Supported Palladium Catalysts Prepared through Atomic Layer Deposition. *ChemElectroChem* **2018**, *5* (5), 743–747. https://doi.org/10.1002/celc.201701196.

(65) Jeevanandam, J.; Barhoum, A.; Chan, Y. S.; Dufresne, A.; Danquah, M. K. Review on Nanoparticles and Nanostructured Materials: History, Sources, Toxicity and Regulations. *Beilstein J. Nanotechnol.* **2018**, *9* (1). https://doi.org/10.3762/bjnano.9.98.

(66) Tan, K.; Barhoum, A.; Pan, S.; Danquah, M. Risks and Toxicity of Nanoparticles and Nanostructured Materials. In *Emerging Applications of Nanoparticles and Architecture Nanostructures*; 2018; pp 121–139.

(67) Smolka, W.; Panek, A.; Gubernat, M.; Szczypta-Fraczek, A.; Jelen, P.; Paluszkiewicz, C.; Markowski, J.; Blazewicz, M. Structure and Biological Properties of Surface-Engineered

Carbon Nanofibers. *J. Nanomater.* **2019**, *2019*, 1–14. https://doi.org/10.1155/2019/4146190.

(68) Lin, H.; Zhang, W.; Shi, Z.; Che, M.; Yu, X.; Tang, Y.; Gao, Q. Electrospinning Hetero-Nanofibers of Fe $_3$ C-Mo $_2$ C/Nitrogen-Doped-Carbon as Efficient Electrocatalysts for Hydrogen Evolution. *ChemSusChem* **2017**, *10* (12), 2597–2604. https://doi.org/10.1002/cssc.201700207.

(69) Liu, Y.; Teng, H.; Hou, H.; You, T. Nonenzymatic Glucose Sensor Based on Renewable Electrospun Ni Nanoparticle-Loaded Carbon Nanofiber Paste Electrode. *Biosens. Bioelectron.* **2009**, *24* (11), 3329–3334. https://doi.org/10.1016/j.bios.2009.04.032.

(70) Maiyalagan, T.; Scott, K. Performance of Carbon Nanofiber Supported Pd-Ni Catalysts for Electro-Oxidation of Ethanol in Alkaline Medium. *J. Power Sources* **2010**, *195* (16), 5246–5251. https://doi.org/10.1016/j.jpowsour.2010.03.022.

(71) Guo, Q.; Liu, D.; Zhang, X.; Li, L.; Hou, H.; Niwa, O.; You, T. Pd–Ni Alloy Nanoparticle/Carbon Nanofiber Composites: Preparation, Structure, and Superior Electrocatalytic Properties for Sugar Analysis. *Anal. Chem.* **2014**, *86* (12), 5898–5905. https://doi.org/10.1021/ac500811j.

(72) Barhoum, A.; García-Betancourt, M. L.; Rahier, H.; Van Assche, G. Physicochemical Characterization of Nanomaterials: Polymorph, Composition, Wettability, and Thermal Stability. In *Emerging Applications of Nanoparticles and Architectural Nanostructures: Current Prospects and Future Trends*; 2018; pp 255–278. https://doi.org/10.1016/B978-0-323-51254-1.00009-9.

(73) Nada, A. A.; Nasr, M.; Viter, R.; Miele, P.; Roualdes, S.; Bechelany, M. Mesoporous ZnFe2O4@TiO2 Nanofibers Prepared by Electrospinning Coupled to PECVD as Highly Performing Photocatalytic Materials. *J. Phys. Chem. C* **2017**. https://doi.org/10.1021/acs.jpcc.7b08567.

(74) El-Sheikh, S. M.; Barhoum, A.; El-Sherbiny, S.; Morsy, F.; El-Midany, A. A.-H.; Rahier, H.

Preparation of Superhydrophobic Nanocalcite Crystals Using Box–Behnken Design. *Arab. J. Chem.* **2019**, *12* (7), 479–1486. https://doi.org/10.1016/j.arabjc.2014.11.003.

(75) Ji, L.; Lin, Z.; Alcoutlabi, M.; Toprakci, O.; Yao, Y.; Xu, G.; Li, S.; Zhang, X. Electrospun Carbon Nanofibers Decorated with Various Amounts of Electrochemically-Inert Nickel Nanoparticles for Use as High-Performance Energy Storage Materials. *RSC Adv.* **2012**, *2* (1), 192–198. https://doi.org/10.1039/c1ra00676b.

(76) Pattanayak, P.; Papiya, F.; Kumar, V.; Pramanik, N.; Kundu, P. P. Deposition of Ni-NiO Nanoparticles on the Reduced Graphene Oxide Filled Polypyrrole: Evaluation as Cathode Catalyst in Microbial Fuel Cells. *Sustain. Energy Fuels* **2019**, *3* (7), 1808–1826. https://doi.org/10.1039/c9se00055k.

(77) Zhu, S.; Sun, J.; Wu, T.; Su, X.; Su, H.; Qu, S.; Xie, Y.; Chen, M.; Diao, G. Graphitized Porous Carbon Nanofibers Prepared by Electrospinning as Anode Materials for Lithium Ion Batteries. *RSC Adv.* **2016**, *6* (86), 83185–83195. https://doi.org/10.1039/C6RA15076D.

(78) Bao, G.; Bai, J.; Li, C. Synergistic Effect of the Pd–Ni Bimetal/Carbon Nanofiber Composite Catalyst in Suzuki Coupling Reaction. *Org. Chem. Front.* **2019**, *6* (3), 352–361. https://doi.org/10.1039/C8QO01100A.

(79) George, G.; Anandhan, S. Synthesis and Characterisation of Nickel Oxide Nanofibre Webs with Alcohol Sensing Characteristics. *RSC Adv.* **2014**, *4* (107), 62009–62020. https://doi.org/10.1039/c4ra11083h.

(80) Di Blasi, A.; Busacca, C.; Di Blasi, O.; Briguglio, N.; Antonucci, V. Synthesis and Characterization of Electrospun Nickel-Carbon Nanofibers as Electrodes for Vanadium Redox Flow Battery. *J. Electrochem. Soc.* **2018**, *165* (7), A1478–A1485. https://doi.org/10.1149/2.1081807jes.

(81) Luo, Q. X.; Guo, L. P.; Yao, S. Y.; Bao, J.; Liu, Z. T.; Liu, Z. W. Cobalt Nanoparticles Confined in Carbon Matrix for Probing the Size Dependence in Fischer-Tropsch Synthesis. *J.*

Catal. **2019**, 143–156. https://doi.org/10.1016/j.jcat.2018.11.002.

(82) Li, M.; Zhu, Y.; Song, N.; Wang, C.; Lu, X. Fabrication of Pt Nanoparticles on Nitrogen-Doped Carbon/Ni Nanofibers for Improved Hydrogen Evolution Activity. *J. Colloid Interface Sci.* **2018**, *514*, 199–207. https://doi.org/10.1016/J.JCIS.2017.12.028.

(83) Sun, J.; Liu, J.; Chen, H.; Han, X.; Wu, Y.; He, J.; Han, C.; Yang, G.; Shan, Y. Strongly Coupled Mo2C and Ni Nanoparticles with In-Situ Formed Interfaces Encapsulated by Porous Carbon Nanofibers for Efficient Hydrogen Evolution Reaction under Alkaline Conditions. *J. Colloid Interface Sci.* **2019**, *558*, 100–105. https://doi.org/10.1016/j.jcis.2019.09.102.